Multichromic Vanadium Pentoxide Thin Films Through Ultrasonic Spray Deposition

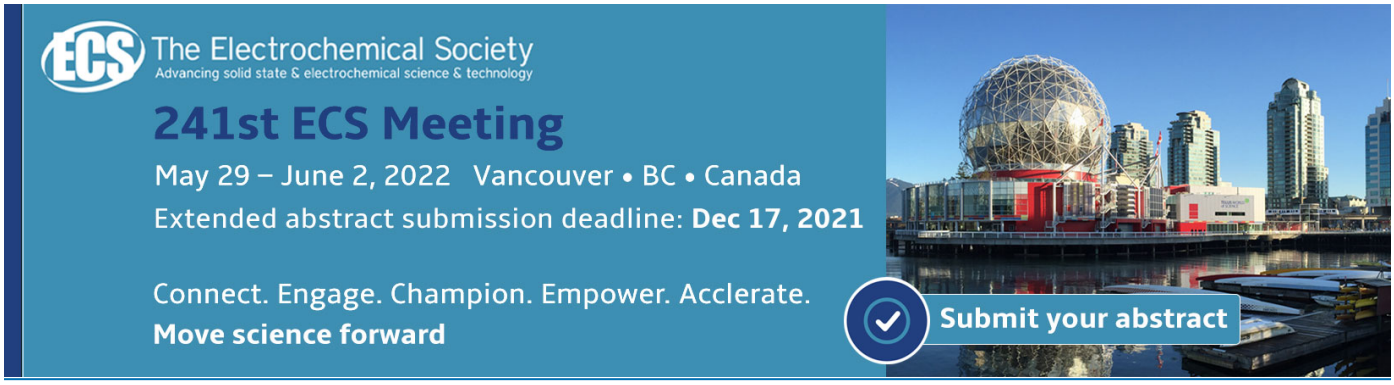

Journal of The Electrochemical Society, 2021 **168** 106511
1945-7111/2021/168(10)/106511/12/$40.00 © 2021 The Electrochemical Society ("ECS"). Published on behalf of ECS by IOP Publishing Limited

Multichromic Vanadium Pentoxide Thin Films Through Ultrasonic Spray Deposition

Yusuf Tutel,[1] Mete Batuhan Durukan,[1,2] Seyma Koc,[1] Serkan Koylan,[1] Huseyin Cakmak,[3] Yusuf Kocak,[4] Farzaneh Hekmat,[5] Emrah Ozensoy,[4,6] Ekmel Ozbay,[3,7] Yasemin Arslan Udum,[8] Levent Toppare,[9] and Husnu Emrah Unalan[1,2,z]

[1]*Department of Metallurgical and Materials Engineering, Middle East Technical University (METU), 06800 Ankara, Turkey*
[2]*Energy Storage Materials and Devices Research Center (ENDAM), Middle East Technical University (METU), 06800 Ankara, Turkey*
[3]*Nanotechnology Research Center (NANOTAM), Bilkent University, 06800, Ankara, Turkey*
[4]*Department of Chemistry, Bilkent University, 06800 Ankara, Turkey*
[5]*Department of Chemistry, Sharif University of Technology, Azadi Avenue, Tehran 11155-9516, Iran*
[6]*UNAM-National Nanotechnology Center, Bilkent University, 06800, Ankara, Turkey*
[7]*Department of Electrical and Electronics Engineering, Bilkent University, 06800, Ankara, Turkey*
[8]*Technical Sciences Vocational School, Gazi University, Ankara, 06500, Turkey*
[9]*Department of Chemistry, Middle East Technical University (METU), 06800 Ankara, Turkey*

Vanadium pentoxide (V_2O_5) is a highly promising material for optoelectronic applications due to its wide optical band gap, significant thermal/chemical stability, and intriguing multichromic properties. Nonetheless, the production of uniform and crack-free V_2O_5 thin films over large areas via conventional deposition methods remain to be a challenge. In this work, we demonstrate deposition of microscopically uniform, large area (15 cm × 15 cm), nanocrystalline and multichromic V_2O_5 thin films onto fluorine-doped tin oxide (FTO) coated glass substrates via ultrasonic spray deposition (USD) method. Thin-film formation behavior, microstructural and optoelectronic properties of the deposited films were investigated as a function of post-deposition annealing temperature. Electrochromic performance of the fabricated films up to an area of 15 cm × 15 cm was monitored using cyclic voltammetry (CV), where 3 different coloration states of V_2O_5 were observed under different applied potentials. Electrochromic devices fabricated with the deposited V_2O_5 thin films were found to be stable up to 1000 cycles. Results presented herein provide a new roadmap for the large area deposition of V_2O_5 through USD method, which can be readily extended to a vast number of other functional metal oxide systems.
 [DOI: 10.1149/1945-7111/ac2dcf]

Manuscript submitted August 14, 2021; revised manuscript received October 1, 2021. Published October 27, 2021.

Supplementary material for this article is available online

Multifunctional thin films have received significant attention due to their potential technological applications. Transition metal oxide thin films have been studied in various fields owing to their tunable physical, optical and electrochemical properties. Among them, vanadium pentoxide (V_2O_5) offers rich oxidation states and long cyclic stability in electrochemical applications.[1,2] Moreover, V_2O_5 thin film electrodes show high chemical stability and reversible color-switching properties. In addition to promising intrinsic properties of V_2O_5 thin film electrodes such as tunable optical band gap, surface porosity, and stability under light, their performance can be altered by changing the morphology and decreasing the grain size down to the nanometer-scale.

Due to the high electrochemical stability of transition metal oxides, they are used in the fabrication of electrochromic devices.[3] Typical examples include, but not limited to, tungsten (VI) oxide (WO_3),[4,5] nickel (II) oxide (NiO)[6,7] and molybdenum (VI) oxide (MoO_3).[8,9] Electrochromic properties of V_2O_5 have gained importance due to its multichromism, where a rapid color change occurs from yellow to blue and green.[10] This rapid color change is associated with the swift intercalation/deintercalation of Li^+ ions within V_2O_5 layers, leading to reversible anodic and cathodic coloration.[11,12]

Vanadium oxides contain vanadium with oxidation states between +2 to +5. V_2O_5 is the most stable phase owing to its large oxygen to vanadium (O/V) ratio and it shows a thermochromic phase transition at 257 °C.[13,14] Amorphous V_2O_5 thin films can be obtained at deposition temperatures below 300 °C,[15] while these disordered V_2O_5 thin films can be crystallized by a simple post-deposition annealing process. V_2O_5 was investigated extensively in the literature due to its unique semiconductor to metal transition behavior, wide optical band gap, high chemical and thermal stability with favorable thermoelectric properties.[15–17] Prototype devices include gas sensors,[18,19] batteries,[20] electrochromic devices,[21,22] and supercapacitors.[23–25] These electronic applications require the deposition of thin, homogeneous, and non-porous films with low resistance, and high carrier diffusion length. Different methods have been utilized for the deposition of V_2O_5 thin films such as thermal evaporation,[26] magnetron sputtering,[27,28] pulsed laser deposition,[29–31] chemical vapor deposition,[32–34] sol-gel,[35,36] spray pyrolysis,[37–39] and ultrasonic spray deposition (USD).[40,41] However, most of the deposition methods are not compatible for deposition over large areas and therefore offer limited scalability. For this reason, there are only a few studies on large area deposition of different types of materials. For instance, Chen et al.[42] demonstrated a continuous roll-coating method for the production of durable VO_2 nanocomposite coatings for smart, energy saving window applications. The utilized method was conducted at a relatively low temperature (240 °C), allowed deposition of films over large areas using solution-based precursors. Ramarajan et al.[43] reported deposition of large area (10 cm × 10 cm) antimony (Sb) doped SnO_2 thin films via spray pyrolysis technique and characterization of its structural, optical, electrical properties and thermal stability. The large area spray deposited Sb-doped SnO_2 thin films showed significant enhancement of the optical and electrical properties with appreciable thermal stability. Among solution-based methods, USD stands out as a simple, inexpensive, and highly advantageous method allowing the deposition of thin films over large areas. Moreover, it offers unique benefits associated with its high material utilization and capability to operate at ambient conditions without any need for low pressures (i.e., vacuum) or elevated temperatures. Besides, it allows reproducible deposition of high purity thin films. Briefly in the USD method, first, a liquid precursor solution is pumped to an ultrasonically excited tip. Then, static waves form in the liquid layer on the surface of the nozzle. These waves eventually become unstable and collapse, causing the formation of fine droplets

[z]E-mail: unalan@metu.edu.tr

of the precursor solution. Finally, the atomized material is carried by a controlled gas flow towards a heated substrate, where it undergoes a thermal decomposition to yield the desired film.

The use of USD method for the deposition of electrochromic thin films has already been demonstrated for NiO[44–46] and WO_3.[47–50] However, to date, only a few studies have investigated the use of USD method for the deposition of V_2O_5 thin films.[40,41] Wei et al. studied electrical and optical properties of V_2O_5 thin films prepared via ultrasonic spraying, where a precursor solution containing hydrogen peroxide and V_2O_5 was used.[40] Furthermore, these films were found to contain mixed phases of V_2O_5 and VO_2, exhibiting a non-uniform morphology due to the stacking of rod-like particles. Tadeo et al. reported synthesis, characterization and humidity sensing properties of polycrystalline V_2O_5 thin films deposited on quartz substrates by ultrasonic nebulized spray pyrolysis of an aqueous combustion mixture.[41] The fabricated humidity sensors based on V_2O_5 thin films showed highly promising response. As can be seen, none of these previous works have investigated the deposition of multichromic V_2O_5 thin films over large areas through USD method.

In this work, we present a direct deposition route for the fabrication of V_2O_5 thin films via USD method onto FTO/glass substrates with a homogeneous, crystalline, crack-free nature. Surface structural, morphological, optical, and electrochromic properties of these single-phase V_2O_5 thin films were comprehensively investigated in the light of post-deposition annealing temperature. The effects of film morphology on electrochromic properties of thin film electrodes and asymmetric cells were explored.

Experimental

Materials.—The FTO/glass substrates were purchased from Hartford Glass Co. (sheet resistance of 21 Ω/square). Vanadyl (IV) acetylacetonate ($VO(acac)_2$, 98%, Sigma Aldrich), vanadium pentoxide (V_2O_5, ⩾ 98%, Sigma Aldrich), and methanol (ACS Reagent, Merck) were used without any purification.

Deposition of thin films.—FTO/glass substrates with different dimensions (i.e., 2 cm × 2 cm, 3.5 cm × 9 cm and 15 cm × 15 cm) were cut and cleaned consecutively by Hellmanex detergent, acetone, isopropanol, and deionized (DI) water for 20 min each at 50 °C using an ultrasonic bath. At the end, samples were dried under N_2 flow.

V_2O_5 films were deposited onto FTO/glass substrates using a commercial USD system (Exacta Coat, Sono-Tek). In the deposition protocol, the concentration of the precursor solution was set to 12.5 mM by dissolving the necessary amount of $VO(acac)_2$ in 50 ml methanol. The methanol-based precursor solution was continuously sprayed through the ultrasonic Vortex nozzle (operated at 120 kHz), which produced stable and conical spray patterns for deposition onto preheated FTO/glass substrates (T = 100 °C). The distance between samples and the spraying nozzle was set at 7 cm. The solution flow rate was 0.1 ml min^{-1} and clean air was used as the carrier gas at 4 kPa. The ultrasonic nozzle was moved in x-y direction following an S-shaped pattern with a 1 mm spacing and at a constant speed of 30 mm s^{-1}. Following deposition, films were annealed at three different temperatures of 450, 500, and 550 °C for 60 min under ambient conditions.

V_2O_5 thin films deposited onto 2 cm × 2 cm FTO/glass substrates were used for morphological, structural, chemical, electrical/electrochemical, and optical characterizations. V_2O_5 thin films deposited on 3.5 cm × 9 cm and 15 cm × 15 cm FTO/glass substrates were used for the fabrication of electrochromic devices with the METU logo and large area, respectively.

Characterization of Thin Films

Structural characterization techniques.—The crystal structure of the deposited films was examined using Rigaku Ultima-IV grazing incidence X-ray diffraction (GIXRD) system equipped with Cu Kα radiation (at a wavelength of 0.154 nm) from 10° to 90° at a scan rate of 1° min^{-1}. X-ray photoelectron spectroscopy (XPS) and Raman spectroscopy were used to examine the surface chemistry and the oxidation state of the elements present in the deposited films. XPS analyses were conducted using a monochromatic Al K_α X-ray source (15 kV, 400 W) with a SPECS PHOIBOS hemispherical analyzer. The nominal binding energy (B.E.) of the C 1 s signal at 284.68 eV was used as a B.E. reference. Raman spectra were recorded with a BRUKER FRA 106/S spectrometer using a 532 nm Nd:YAG laser excitation source. A spectroscopic ellipsometer was used to determine the thickness of the thin films on a Woollam, M2000V instrument. In order to improve fitting precision, data were collected at 3 different angles of 65, 70 and 75°.

Morphological characterization of thin films.—Scanning electron microscopy (SEM) analyses were conducted in order to investigate the microstructure of the deposited thin films. An FEI Nova Nano FEG-SEM equipped with an energy dispersive X-ray (EDX) analyzer operated at 20 kV was used for this purpose. A thin Au layer was deposited onto the samples prior to SEM and EDX analysis. Atomic force microscopy (AFM) was utilized to monitor the surface morphology of the films. A Veeco MultiMode V AFM was used in tapping mode.

Electrical and optical characterization of thin films.—The Hall effect measurements were conducted at room temperature using an Ecopia HMS3000 system to determine the charge carrier density and charge mobility of the thin films on quartz substrates. UV–visible light transmission of the films was recorded within 200−1000 nm using a PG T80 + UV–Vis Spectrophotometer, where FTO/glass substrates were used as a background.

Electrochemical characterization of thin films.—A Biologic VMP3 potentiostat/galvanostat system was utilized for the electrochemical characterization. To understand the electrochemical behavior of V_2O_5 thin films, cyclic voltammetry (CV) analyses were performed in a 3-electrode setup within a potential range of −2.0 V to 2.0 V relative to Ag/AgCl reference electrode in saturated potassium chloride (KCl). Platinum foil was used as the counter electrode and 1 M lithium perchlorate ($LiClO_4$) in propylene carbonate (PC) was used as the electrolyte. Potentiostatic impedance analysis (PEIS) was conducted at a frequency range of 200 kHz to 50 mHz with an amplitude of 20 mV and an applied potential of 0.05 V. Spectroelectrochemical studies of V_2O_5 thin films were carried out using lithium perchlorate ($LiClO_4$) electrolyte via a Varian Cary 5000 UV–Vis spectrophotometer.

Electrochromic cells were fabricated to check the cyclic stability and large-scale colorations. The cycling performance of the V_2O_5 thin films was monitored by assembling an asymmetric cell, where deposited V_2O_5 thin films on FTO and bare FTO acted as the anode and cathode, respectively. These two layers were assembled using a 3 M VHB band, which also ensured the encapsulation of the cell. Then, 1 M $LiClO_4$ in PC was filled into the encapsulated cell with the help of a syringe to finalize the assembly of an asymmetric electrochromic cell. The same protocol was utilized in the fabrication of 15 cm × 15 cm electrochromic cells.

To pattern V_2O_5 thin films by ablating excess V_2O_5 and FTO on the glass substrates, FiberLAST-NanoMark Energy Series (20 W, 1064 nm wavelength, 100 ns pulse length) nanosecond laser marking system was used. Excess V_2O_5/FTO was removed with a power, frequency, and marking speed of 10 W, 50 kHz, and 100 mm s^{-1}, respectively. Then, 4 W of power with the same frequency and marking speed as before was used to remove V_2O_5 overcoat to expose the FTO contacts for separate colorations of the letters. Lastly, two electrode asymmetric cells were fabricated with the same procedure as above for colorations.

Results and Discussion

Structural properties.—The average thicknesses of as-deposited and V_2O_5 thin films annealed at 450, 500, and 550 °C were

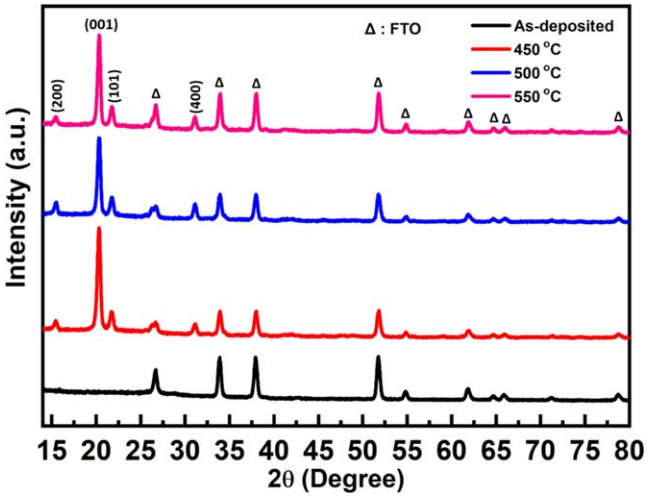

Figure 1. XRD patterns of as-deposited V_2O_5 thin films and films annealed at different temperatures.

determined using ellipsometry as 62, 69, 74, and 76 nm, respectively. The thickness of the thin films was found to increase with the annealing temperature.[51] The increase in film thickness was attributed to grain growth.

XRD patterns of the V_2O_5 thin films, provided in Fig. 1 showed that as-deposited films were amorphous, while thin films annealed at 450, 500, and 550 °C had an orthorhombic structure (PDF 00-041-1426) with 2θ values of 15.4°, 20.3°, 21.4°, and 31.1° indexed to (200), (001), (101), and (400) planes, respectively.[52–55] Furthermore, annealed films showed a *c*-axis preferred orientation, where the (001) planes lied parallel to the substrate.

The crystallite size, strain and dislocation density, obtained from XRD profiles using (001) peak are tabulated and provided in Table I. The average crystallite sizes (D) of annealed V_2O_5 thin films at temperatures of 450, 500, and 550 °C were found to increase slightly from 20.1 to 22.3 nm, which were calculated using the Scherrer's equation ($D = 0.94\lambda/\beta\cos\theta$). Herein, λ refers to the wavelength of the X-ray, β is the full width at half maximum (FWHM) and θ is the Bragg angle. The slight increase in crystallite size with increasing post-deposition annealing temperatures might be attributed to the grain growth process. The strain (ε) and dislocation density (δ) were calculated using relations $\varepsilon = (\beta\cos\theta)/4$[56] and $\delta = 1/D^2$,[57] respectively.V_2O_5thin film annealed at 450 °C (i.e., the best performing thin film in the current work) showed the highest values of strain and dislocation density as compared to the rest of the investigated films.

Vibrational structure of the deposited V_2O_5 films on FTO/glass substrate along with that of a commercial V_2O_5 powder benchmark sample were studied using Raman spectroscopy (Fig. 2). It can be seen in Fig. 2a that V_2O_5 powder benchmark sample and the V_2O_5 thin films revealed similar Raman features located at ca. 144, 196, 283, 404, 481, 527, 701, 996 cm^{-1}. Considering the fact that the currently deposited V_2O_5 thin films had a thickness within 60 − 80 nm, one can argue that the Raman spectra of the currently investigated thin films contained both surface and bulk-related Raman signals. In a detailed study, Baddour-Hadjean et al. reported that crystalline V_2O_5 thin films with a thickness of 600 nm (i.e., much thicker than the currently investigated vanadia films) revealed the following experimentally detectable Raman signals: i) 994 cm^{-1} (ν(V–O), A_g, stretching), ii) 700 cm^{-1} (ν(V–O), B_{1g} and B_{3g}, stretching), iii) 526 cm^{-1} (ν(V–O), A_g, stretching), iv) 480 cm^{-1} (δ(V–O–V), A_g, bending), v) 403 cm^{-1} (ρ(V = O), A_g, rocking), vi) 302 cm^{-1} (ρ(V = O), A_g, rocking), vii) 282 cm^{-1}(ρ(V = O), $B_{1g}$and B_{3g}, rocking), viii) 195 cm^{-1} (δ(O–V–O), A_g and B_{3g}, bending), and ix) 144 cm^{-1} (δ(O–V–O), $B_{1g}$and B_{3g}, bending) where the assignments were based on the bulk V_2O_5 lattice structure.[58] Raman spectra of the V_2O_5 thin films given in Fig. 2a indicate close resemblance to these modes suggesting the presence of a bulk-like V_2O_5 structure in the films. This is also evident by the strong Raman signal at 144–152 cm^{-1} (Figs. 2a and 2b) suggesting the presence of long-range structural order.[58] On the other hand, the unique frequency shift in this latter Raman signal for the V_2O_5 thin film annealed at 450 °C (which is also the best performing thin film structure in the current work) reveals important structural dissimilarities as compared to all other currently investigated thin films (Fig. 2b). Based on the literature data,[58] it can be argued that the unique shift in this Raman signal can be associated with the structural differences and relative disordering in the thin film annealed at 450 °C due to variations in the shear motion of the vanadia ladders[58] (i.e., B_{1g} mode) and the alterations in the rotations of the ladders along their axes[58] (i.e., B_{3g} mode). This argument is also consistent with the difference in the FWHM value of this feature for the thin film annealed at 450 °C (i.e., FHWM = 10.0 cm^{-1}) as opposed to that of the films annealed at 500 °C and 550 °C (i.e. FHWM = 8.8 cm^{-1}).

In light of a recent comprehensive review,[59] we can also briefly discuss the possible contribution of VO_x surface functionalities in the Raman spectra given in Fig. 2. Particularly, the high-frequency Raman signals at >800 cm^{-1} can be informative allowing the unambiguous identification of the various VO_x surface functional groups (e.g., VO_4, orthovanadate; V_2O_7, pyrovanadate; $(VO_3)_n$ metavanadate; $V_{10}O_{28}$, decavanadate; and V_2O_5 nanoparticles, NP). Along these lines, V–O stretching signal at 996 cm^{-1} in the Raman spectra in Fig. 2a may also suggest the presence of V_2O_5 NP and V_2O_5 microcrystallites.[59] The characteristic Raman mode at 996 cm^{-1} has been typically observed for both hydrated (i.e., exposed to ambient conditions before spectral acquisition) or dehydrated (i.e., annealed in the absence of air and not exposed to ambient conditions before spectral acquisition) V_2O_5 films containing ordered vanadium pentoxide NPs deposited on numerous metal oxides (e.g. TiO_2, ZrO_2, SiO_2 etc.).[13,60–62] Occurrence of very weak shoulder signals at 1005 and 1010 cm^{-1} (Fig. 2c) for the vanadia thin film annealed at 450 °C suggests the possible presence of decavanadate ($V_{10}O_{28}$) and/or isolated mono-oxovanadate (VO_4) surface functional groups as additional minority species, respectively,[62] where these features are not expressed for the films annealed at 500 °C and 550 °C.

V_2O_5 thin film annealed at 450 °C was also analyzed with XPS in order to investigate its electronic structure in detail (Figs. 3 and S1 available online at stacks.iop.org/JES/168/106511/mmedia). XPS method is extensively used to characterize vanadia thin films in the literature.[63–69] The most intense XPS signal of vanadia overlayers is the V2*p* feature. Due to the complex electronic interactions (hybridization effects on V2*p* and the closely located O1*s* signals[66] as well as the existence of additional loss and satellite features[64]), interpretation of the vanadium oxidation state via XPS is not trivial. In a comprehensive study by Silversmit et al.,[66] it was reported that V2$p_{3/2}$ signals for V^{5+},

Table I. Microstructural parameters for V_2O_5 films annealed at various temperatures.

Annealing T (°C)	(hkl)	Crystallite Size (nm)	Strain (10^{-3} lin.$^{-2}$m^{-4})	Dislocation Density (10^{14} lin.m^{-2})
450	(001)	20.1	1.8	24.7
500	(001)	21.1	1.7	22.4
550	(001)	22.3	1.6	20.0

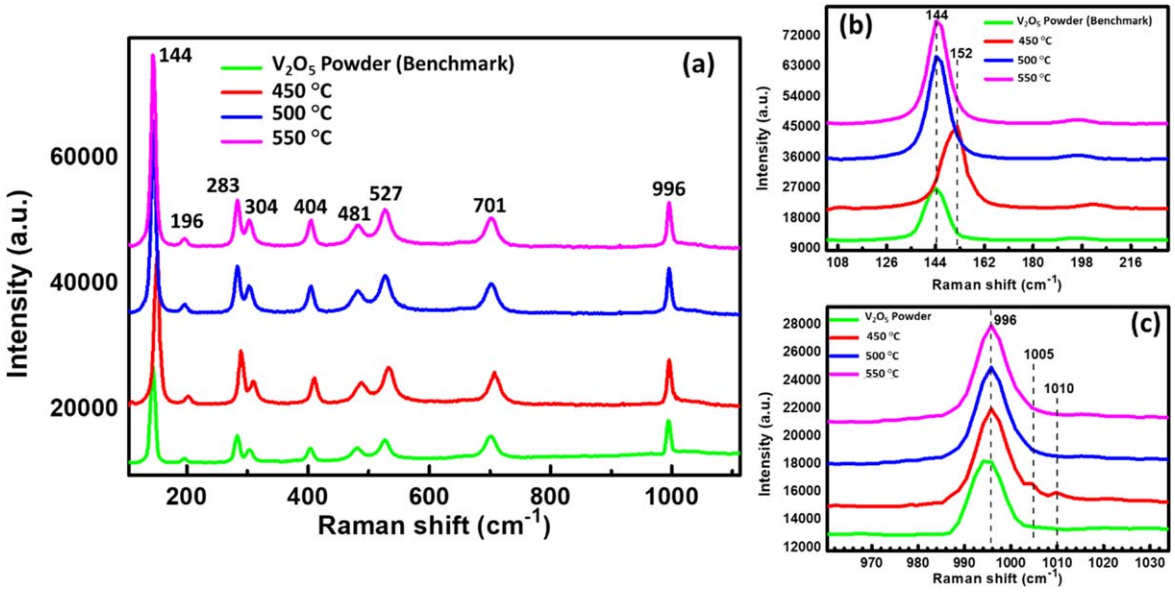

Figure 2. (a)–(c) Raman spectra of commercial V_2O_5 powder and V_2O_5 thin films annealed at different temperatures.

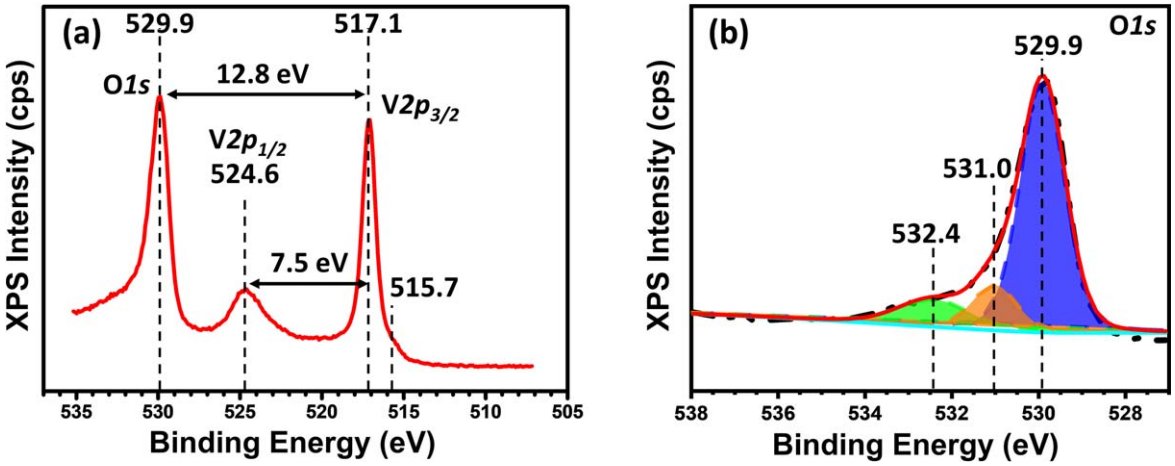

Figure 3. XPS data of the V_2O_5 thin film annealed at 450 °C. (a) V2*p* and O*1s*, (b) O*1s* binding energy regions.

V^{4+}, V^{3+}, V^{2+}, V^0 states were observed at 517.2, 515.8, 515.3, 513.7, 512.4 eV, respectively. Furthermore, it was shown by Zimmerman et al.[64] that the binding energy (B. E.) difference between O*1s* and V$2p_{3/2}$ states (i.e., Δ = B.E. (O*1s*)-B.E.(V$2p_{3/2}$) could also be used as an additional effective parameter for the reliable assessment of various vanadium oxidation states. In the light of this information, V$2p_{3/2}$ XPS spectrum of the vanadia film annealed at 450 °C given in Fig. 3a can be interpreted. Figure 3a shows that in addition to the major O*1s* signal at 529.9 eV, three different V2*p* XPS signals are observed at 524.6, 517.1, and 515.7 eV, which can be attributed to $V^{5+}2p_{1/2}$, $V^{5+}2p_{3/2}$, and $V^{4+}2p_{3/2}$ states in very good accordance with the literature, respectively.[66] It should be emphasized that in addition to the particular B.E. position of the $V^{5+}2p_{3/2}$ signal, Δ value of 12.8 eV as well as the spin–orbit splitting between $V^{5+}2p_{1/2}$ and $V^{5+}2p_{3/2}$ signals (i.e., 7.5 eV) are also in perfect agreement with the assignment that the predominant vanadia phase of the film annealed at 450 °C is V_2O_5 revealing a vanadium oxidation state of +5.[66] While the V^{5+} state (i.e., V_2O_5) is by far the most prominent feature in Fig. 3a, there also exists a very weak yet discernible shoulder feature at 515.7 eV which can be assigned to the presence of minuscule quantities of V^{4+} species. This is also in excellent harmony with the currently presented Raman data of this film (Figs. 2b–2c) revealing slightly disordered V_2O_5 NP as the predominant species along with decavanadate ($V_{10}O_{28}$) and/or isolated mono-oxovanadate (VO_4) surface functional groups as minority species. Thus, based on the XPS data given in Fig. 3a, it can be argued that the thin film prepared by annealing at 450 °C is mostly comprised of V^{5+} species with an extremely small contribution from V^{4+} species.

Additional information can also be gathered by analyzing the O*1s* XPS signals of the V_2O_5 thin film annealed at 450 °C (Fig. 3b). Deconvolution of the asymmetric O*1s* signal in Fig. 3b yields three distinct O*1s* features at 529.9, 531.0, 532.4 eV. The most prominent O*1s* signal at 529.9 eV can be readily assigned to V–O species in the vanadia film.[63–69] The shoulder feature appearing at 531.0 eV has been discussed in detail by Silversmit et al.[66] and can be attributed to a $V^{5+}2p_{3/2}$ satellite. It should be noted that the O*1s* signal at 531.0 eV can also have a minor contribution from the SnO_x species of the FTO substrate,[70] whose Sn*3d* signal is also visible in the survey XPS spectrum of this sample (Fig. S1). Finally, the minor feature with a high B.E. O*1s* signal at 532.4 eV can be assigned to C=O/C–O(H) residual organic oxygenates on the surface, whose origin is most likely associated to the anionic component (or its oxidized forms) of the vanadyl (IV) acetylacetonate precursor used in the thin film synthesis.

Morphology of thin films.—SEM and AFM analyses revealed the surface morphology of the deposited films (Fig. 4). SEM image

of the as-deposited film (Fig. 4a) is almost featureless with a relatively smooth surface. This characteristic amorphous surface has a low root mean square (RMS) roughness value as shown in Figs. 4b–4c. Upon annealing the films at 450, 500, and 550 °C, as a result of oxidation and sintering, corrugated features started to appear as shown in Figs. 4d, 4g, and 4j, respectively. Observations of ordered nanorod structures in SEM images are consistent with the XRD, Raman, and XPS results (Figs. 1–3). 3D AFM profiles and phase maps for thin films annealed at 450, 500, and 550 °C are shown in Figs. 4e–4f, 4h–4i, and 4k–4l, respectively. The size of the nanorods is found to increase with the annealing temperature. At an annealing temperature of 550 °C, the morphology of the nanorods started to degrade, where they coalesced with each other. The RMS roughness values for the as-deposited as well as 450, 500, and 550 °C annealed V_2O_5 films are measured as 5.2, 12.5, 15.8, 17.2 nm, respectively. With an increase in the annealing temperature from 450 to 550 °C, RMS roughness values of the films are found to increase. The AFM images are in good agreement with the currently presented characterization results (Figs. 1–3), suggesting that the crystalline domains form at an annealing temperature of 450 °C, and grow in size with increasing annealing temperature. It should also be noted that in addition to its simplicity and structural uniformity of the deposited films at the microscopic level, USD method enabled the deposition of thin films over large areas (e.g., 15 cm × 15 cm), as shown in **Fig. S2.**

Electrical and optical properties.—Hall-effect measurements were conducted at room temperature to evaluate charge carrier concentration, resistivity, and mobility of the thin films. Obtained results are tabulated and presented in Table II. Measurements

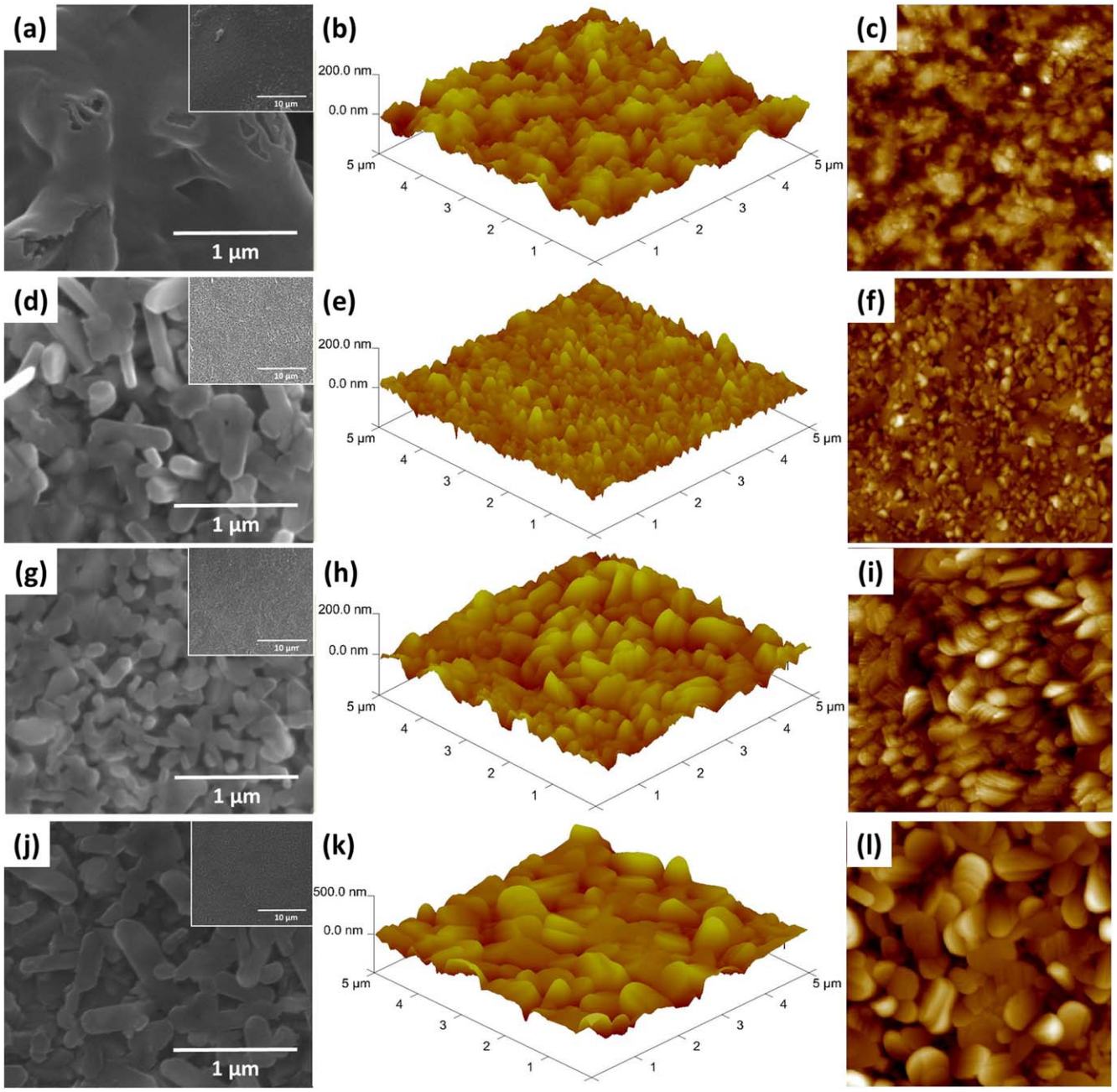

Figure 4. Surface morphology of deposited V_2O_5 thin films via SEM are shown in the images on the left column. Images in the middle column show 3D AFM maps, while images on the right column present AFM phase maps. (a)–(c) as-deposited sample, samples annealed at (d)–(f) 450 °C, (g)–(i) 500 °C, and (j)–(l) 550 °C.

showed that all films were *n*-type semiconductors. As-deposited thin film showed a relatively low carrier concentration (6.85×10^{12} cm^{-3}), but high mobility (5.80 cm^2 V^{-1} s), and resistivity (1.57×10^5 Ω cm) compared to the annealed films. Carrier concentration and resistivity values are found to be quite similar to the V_2O_5 films annealed at 450 and 500 °C. Upon annealing at 550 °C, carrier concentration was found to increase almost four times, and resistivity was found to decrease slightly. Mobility increased with an increase in the annealing temperature. Variations in resistivity, carrier concentration, and mobility values might be explained by the changes in dislocation densities upon annealing. As dislocation density increases, various types of defects trap the carriers and lower the free carrier concentration and mobility.[71,72] Thus, carrier concentration increased dramatically for the V_2O_5 films annealed at 550 °C. Furthermore, crystallite size calculated using Scherrer equation from XRD increased with the annealing temperature, which resulted in an increase in carrier mobility.

The optical transmission spectra of the films are provided in Fig. 5. At a wavelength of 600 nm, the optical transmittance of as-deposited thin films was approximately 92%, while that of annealed films at 450, 500, and 550 °C were 83%, 73%, and 69%, respectively. Besides, approximately a 5%–7% increase in transmittance was observed for all films in the near-infrared region. As discussed through the AFM images, annealing temperature increases the surface roughness, which eventually increases light scattering and decreases the optical transmittance.[38] Moreover, annealing temperature dependent increase in film thickness and grain size can also lead to a decrease in the transmittance of the films.[73–75]

The optical band gap values of V_2O_5 films were determined via UV–vis spectroscopy measurements using Tauc's relation,

$$\alpha h\nu = A(h\nu - E_g)^m,$$

where α is the absorption coefficient obtained from Lambert formula, $h\nu$ is the incident photon energy, A is the characteristic constant independent of photon energy, E_g is the optical band gap and m is an index that can have different values such as 1/2, 3/2, 2 or 3 depending on the nature of the electronic transitions. The variation of $(\alpha h\nu)^2$ vs $h\nu$ for V_2O_5 films annealed at 450, 500, and 550 °C is provided in the inset of Fig. 5. E_g values of the films are estimated through extrapolating the linear portion of the plots. Band gap values of 2.69, 2.63, and 2.58 eV are obtained for films annealed at 450, 500, and 550 °C, respectively. E_g values are found to decrease only marginally with increasing annealing temperature, and Yelsani et al. and Madhuri et al. reported similar behavior of optical band gap. Yelsani et al. showed the decrease in *Eg* values from 2.40 to 2.14 eV, upon post-annealing treatment of V_2O_5 films deposited via spray pyrolysis method.[73] Moreover, Madhuri et al. showed that the increased substrate temperature decreased band gap of V_2O_5 films deposited by the electron beam evaporation method.[28] Reduction in the optical band gap values might be tentatively attributed to increased average crystallite size and decreased strain upon increasing the annealing temperature.

Electrochromic properties.—Electrochromic performance of the V_2O_5 thin films was investigated both in 3-electrode and asymmetric cell setup to understand the effects of porous morphology, where V_2O_5 and bare FTO were utilized as positive and negative

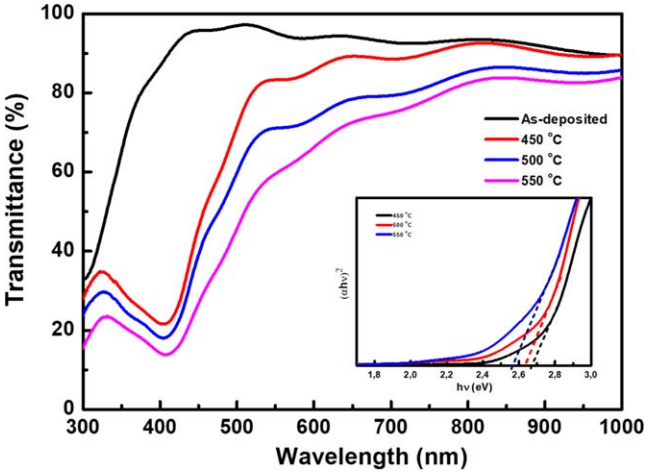

Figure 5. Transmittance spectra for as-deposited and annealed V_2O_5 thin films. Inset shows corresponding Tauc plots obtained from UV–vis spectroscopy measurements.

electrodes, respectively. Cyclic voltammograms of the V_2O_5 films annealed at 450, 500, and 550 °C in 3-electrode setup were obtained (Fig. 6) to understand the electrochemical behavior of the films after 5 cycles. For the annealed films, the color of the electrodes was initially yellow and then turned into blue at the reduced state. The change in the color occurred according to the reaction given below, which includes intercalation/deintercalation of Li^+ ions into/from V_2O_5 thin films. Note that the source of the Li^+ ions was the lithium perchlorate ($LiClO_4$) in propylene carbonate (PC) solution, which was used as the electrolyte in the electrochemical setup.

$$V_2O_5(Yellow) + xLi + +xe - = Li_xV_2O_5(Blueish\ Green)$$

Photos of color changes are provided as insets within the CV curves provided in Fig. 6a. Cathodic peaks (around −1.5 and −0.4 V) in the voltammograms were due to Li^+ intercalation into the V_2O_5 structure, while the anodic peaks (around 1.2 and 1.7 V) were attributed to Li^+ deintercalation from the films.[76] While the anodic region contained only V^{4+} and V^{5+}, first cathodic reduction around −0.5 V resulted in a mixed state of V^{5+}, V^{4+}, and V^{3+}, which turned the as-deposited V_2O_5 into olive green.[21] Reduction via Li^+ insertion into V_2O_5 structure lowered the valence of as-deposited yellowish pentavalent vanadium (V^{5+}) to a mixed state of V^{4+} and V^{3+}, with an increased ratio of V^{3+} after −1 V, resulting in a blueish green color.[77–79] Increased cathodic polarization up to −1.5 V brought further conversion to V^{3+} valence state, resulting in a conversion of green color into a blueish green. Upon the application of anodic potentials, conversion to yellow color (similar to the color of as-prepared V_2O_5) occurred, indicating the deintercalation of V_2O_5 crystal. Further polarization around 1.7 V increased the oxidation state of vanadium ions with a brownish-orange coloration.[78]

The degree of crystallization in thin films is of great importance in determining the electrochromic (EC) performance. EC performance depends on the crystal structure as the conduction of ions occurs between the octahedral sites of the crystalline V_2O_5. Broad

Table II. Hall-effect measurement results of as-deposited and annealed V_2O_5 thin films.

Annealing T (°C)	Carrier concentration (cm^{-3})	Mobility (cm^2/V.s)	Resistivity (Ω.cm)	Type
As-deposited	6.8×10^{12}	5.8×10^{0}	1.6×10^{5}	n
450	7.9×10^{17}	6.0×10^{-1}	13.3	n
500	9.8×10^{17}	6.8×10^{-1}	9.4	n
550	3.5×10^{18}	1.2×10^{0}	3.9	**n**

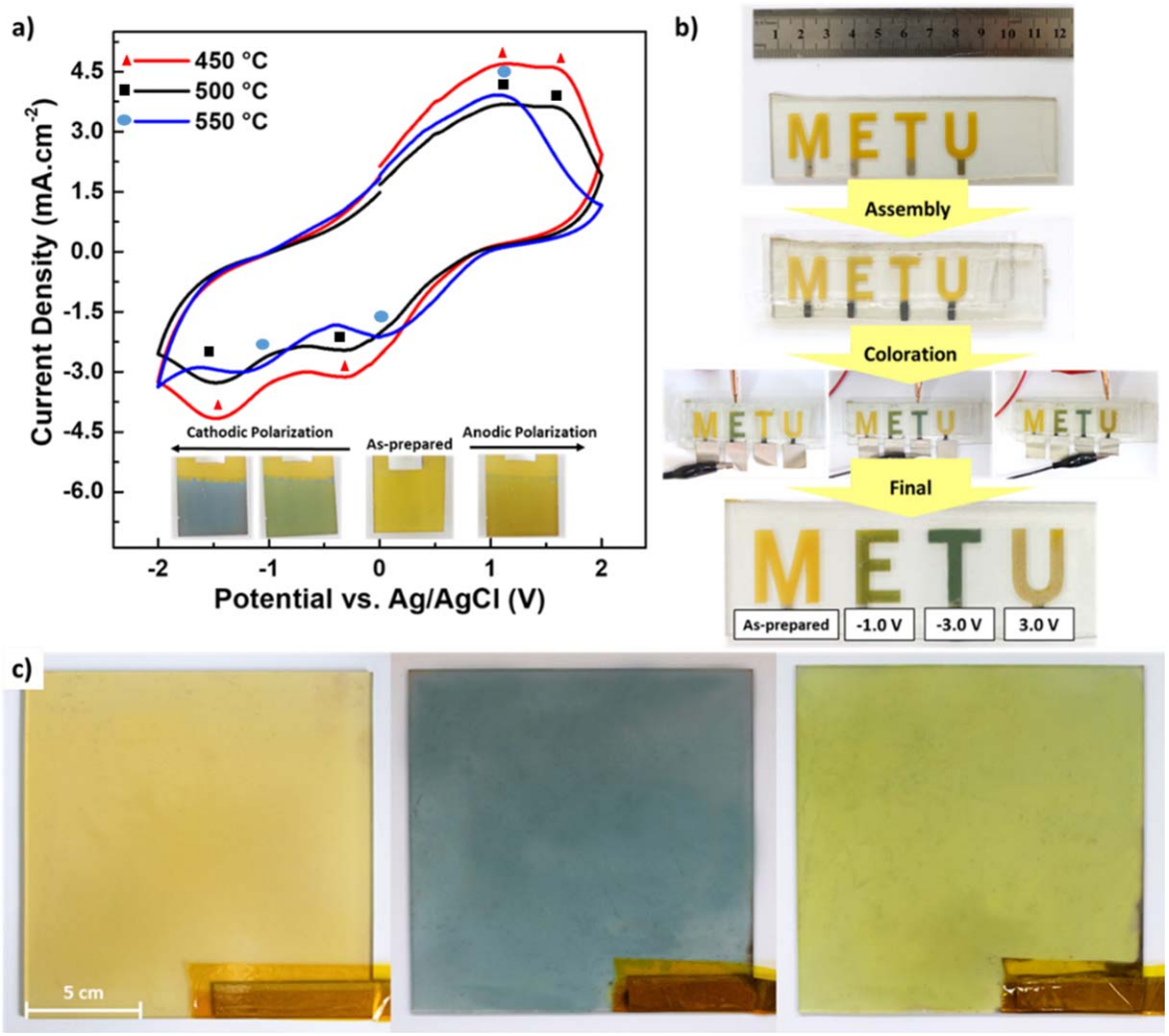

Figure 6. (a) Cyclic voltammograms of V_2O_5 thin films annealed at different temperatures at a scan rate of 100 mV s^{-1} in a 3-electrode setup. Insets show the photographs of thin films at different oxidation states. (b) Photographs of patterned electrochromic film in different states and final coloration states of V_2O_5 thin film demonstrating the potential of the USD method and multichromic V_2O_5. (c) Photographs of the large area (15 cm × 15 cm) electrochromic films in as-prepared (left) and colored states (middle and right).

reduction and oxidation peaks can be attributed to the nanostructured V_2O_5 thin films. Here, decreased current density of the intercalation/deintercalation peaks for the 500 °C annealed film with respect to that of 450 °C shows the reduced activity of vanadium sites. Especially annealing the samples at 550 °C resulted in narrower intercalation/deintercalation peaks, further confirming the decreased performance due to degradation of the nanorod morphology. Using the cyclic voltammograms, it was possible to deduce that the film annealed at 450 °C had the highest number of active vanadium sites, which corresponds to an increased diffusion coefficient of Li^+ according to the equation below;[80]

$$i_p = (2.69x10^5)n^{\frac{3}{2}}AD_{Li}^{\frac{1}{2}}C_{Li}^{*}v^{\frac{1}{2}},$$

where i_p is the peak current or peak current density (A or A cm^{-2}), A is the electrode area (cm^2), D_{Li} is the diffusion coefficient of Li^+ into the V_2O_5 structure (cm^2 s^{-1}), C_{Li} is the ionic concentration in the electrolyte (mol cm^{-3}), and v is the potential scan rate (V s^{-1}). According to this equation, it is evident that the increased current density of the V_2O_5 corresponds to an increased diffusion coefficient for the Li^+ intercalation/deintercalation. By using cyclic voltammograms, the diffusion coefficient of Li^+ ions into the V_2O_5 thin films annealed at 450 °C was estimated to be 3.01 × 10^{-9} cm^2 s^{-1} at a scan rate of 100 mV s^{-1}. This is one of the best values obtained recently.[12,81–83] Low diffusion coefficient for Li ions resulted in a decrease in peak currents for the samples annealed at 500 °C and 550 °C, which were estimated to be 2.14 × 10^{-9} and 1.87 × 10^{-9} cm^2 s^{-1}, respectively. The decrease in diffusion coefficient with temperature was attributed to the bulky structure of V_2O_5 upon annealing at higher temperatures, as discussed through Raman results and the degradation of nanorod morphology at elevated temperatures as verified by the AFM and SEM images (Fig. 4).

V_2O_5 films were laser ablated to obtain individual letters to conceptualize the multichromic behavior. The steps and the photographs of the assembly and coloration of the patterned film are provided in Fig. 6b. Following the formation of the letters via laser ablation, bare FTO was also laser ablated to divide it into 4 parts to obtain 4 separated cells, each containing a single letter. Then, the enclosed cell was filled with electrolyte, ultimately forming an electrochromic cell, where V_2O_5 and bare FTO act as anode and cathode, respectively. Consequently, each letter was subjected to a constant voltage to obtain different colors. Applied voltages are −1, −3, and 3 V to letters "E", "T", and "U", respectively. Letter "M" was left in the as-prepared condition for comparison. To practice the feasibility of USD method for fabricating large-scale electrochromic films, V_2O_5 thin films were also deposited over large areas (15 cm × 15 cm), and the coloring was practiced through a large bare FTO

substrate as the cathode. The assembled asymmetric cell was again filled with 1 M $LiClO_4$ in PC electrolyte. Photographs of the colored states of the electrochromic film are provided in Fig. 6c. While the large-scale coloration was successfully achieved, homogeneity of the films in as-prepared, blue, and green states was assessed by evaluating the RGB (red, green, blue) color codes in pre-defined areas (**Fig. S3**). Detailed information on this procedure can be found in the supporting information section. By calculating the mean and the standard deviation of the RGB color codes, the coefficient of variation was calculated and provided in **Table SI**. A maximum coefficient of variation of 9.1% was observed in these measurements, confirming the uniformity and homogeneity of the thin films deposited through USD method over large areas.

Figure S4 shows the PEIS results of as-deposited and annealed V_2O_5 films at 450, 500, and 550 °C. The starting point of the high-frequency region in the spectrum corresponds to the series resistance. It is evident that annealing lowers the resistance of the as-deposited film, offering better conductivity (inset of Fig. S4). Annealing at 450 °C and 500 °C offers the best results in terms of conductivity. When compared, thin-film annealed at 450 °C has a very small semi-circular region, proving its better kinetic activity when compared to the film annealed at 500 °C. From the slope of the low-frequency region, it is possible to deduce that the electrochromic reactions in as-deposited film are more diffusion-limited compared to the annealed ones.

Transmittance changes of the films were monitored in colored (obtained with 2 V bias) and bleached (obtained with −2 V bias) states (Fig. 7). There was no change in the transmittance for amorphous films in accordance with the former studies in the literature, where electrochromic response was reported only for the orthorhombic crystals.[84,85] A maximum transmittance change of 18% was obtained at a wavelength of 900 nm for the films annealed at 450 °C. Changes in transmittance values were found to decrease with increasing annealing temperature. Maximum transmittance changes of 11% and 7% were obtained for the films annealed at 500 and 550 °C at a wavelength of 900 nm, respectively.

Cyclic stability of the coloration of V_2O_5 thin films annealed at 450, 500, and 550 °C was evaluated by switching between bleached and colored states at a wavelength of 405 nm ± 1 nm. Figure 8 shows the switching behaviors of as-deposited and 450, 500, and 550 °C annealed V_2O_5 thin films. There was no significant transmittance change (ΔT) between bleached and colored states for as-deposited thin films as provided in Fig. 7a. On the other hand, ΔT was observed around 17%, 15%, and 4% for thin films annealed at 450, 500, and 550 °C, respectively. The stability test lasted for 300 s over 25 switching cycles. The annealed thin films showed consistent transmittance values, whereas ΔT of as-deposited thin films decreased gradually. In addition, Table III shows the comparison of important electrochromic parameters with those in literature. Our results are comparable with the other studies.[22,86–88]

Chronocoulometric (CC) and chronoamperometric (CA) measurements were used to directly compare the charge efficiencies and chronoamperometric behavior during the insertion and extraction of lithium ions. Each electrode was first biased at +2.0 V vs a Ag/AgCl reference electrode to remove the adsorbed Li^+ ions from the electrode surface. The polarity was then switched immediately to −2.0 V to initiate lithium intercalation, then switched back to +2.0 V to observe the deintercalation behavior. The change in both the charge and current densities were collected and provided in Fig. 9. As can be seen from the graphs, the 450 °C annealed sample showed the highest charge density in the same time domain, further proving its higher diffusivity (Figs. 9a–9c–9e). This case is further demonstrated in **Fig S5a**, where the CC comparison of the 2nd cycle of intercalation and deintercalation is provided. While the difference between 450 °C and 500 °C annealed samples is smaller (which is consistent with the CV curves provided in Fig. 6a), 550 °C annealed sample showed much small charge densities. This can be attributed to the aforementioned degradation in the nanorod morphology with the increase in annealing temperature. The

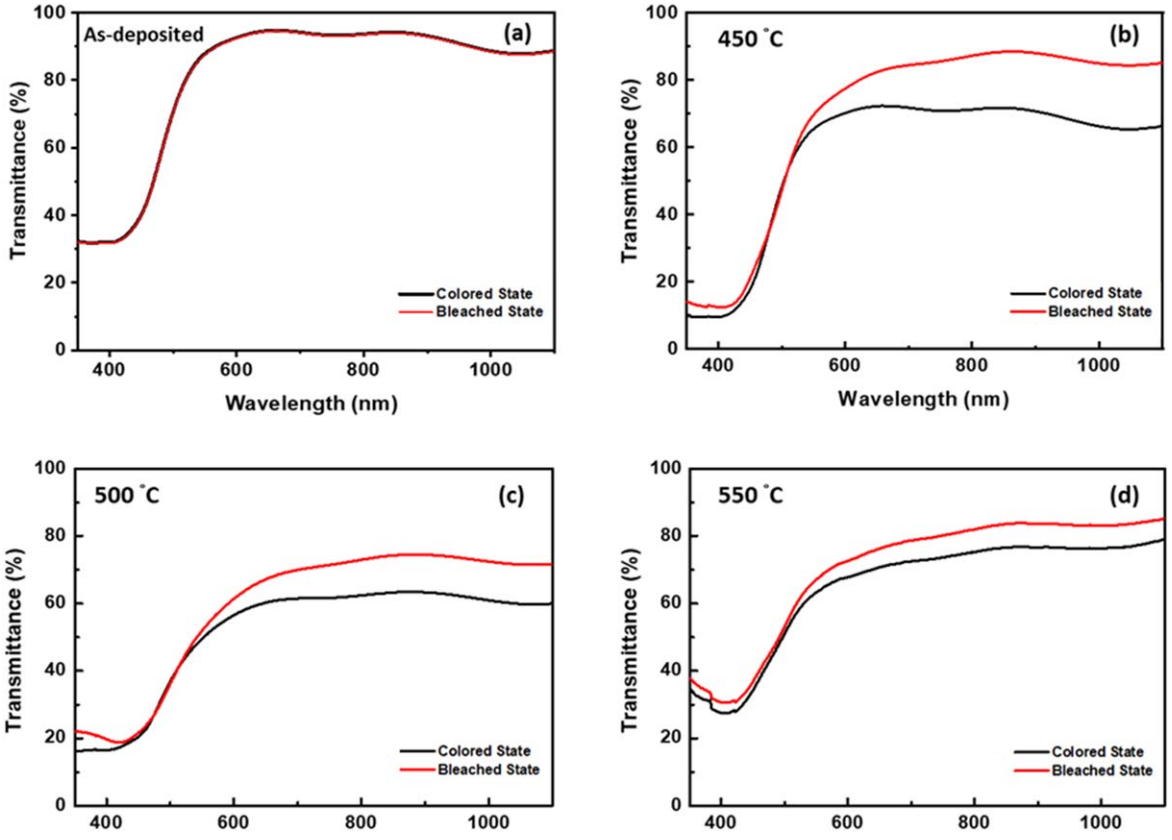

Figure 7. Transmittance spectra for (a) as-deposited and (b) 450 °C, (c) 500 °C, and (d) 550 °C annealed V_2O_5 thin films in colored and bleached states.

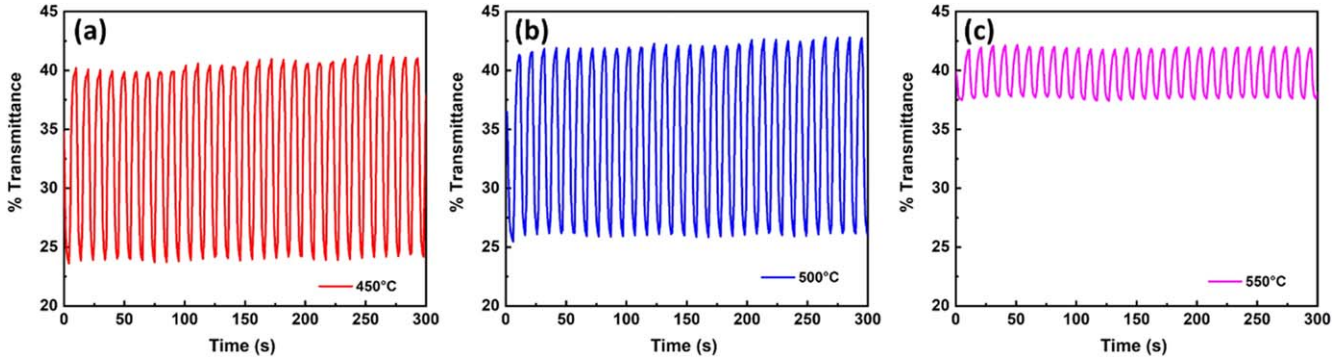

Figure 8. Electrochromic cyclic stability test results and changes in optical transmittance for (a) 450 °C, (b) 500 °C and (c) 550 °C annealed V_2O_5 thin films upon switching between bleached and colored states.

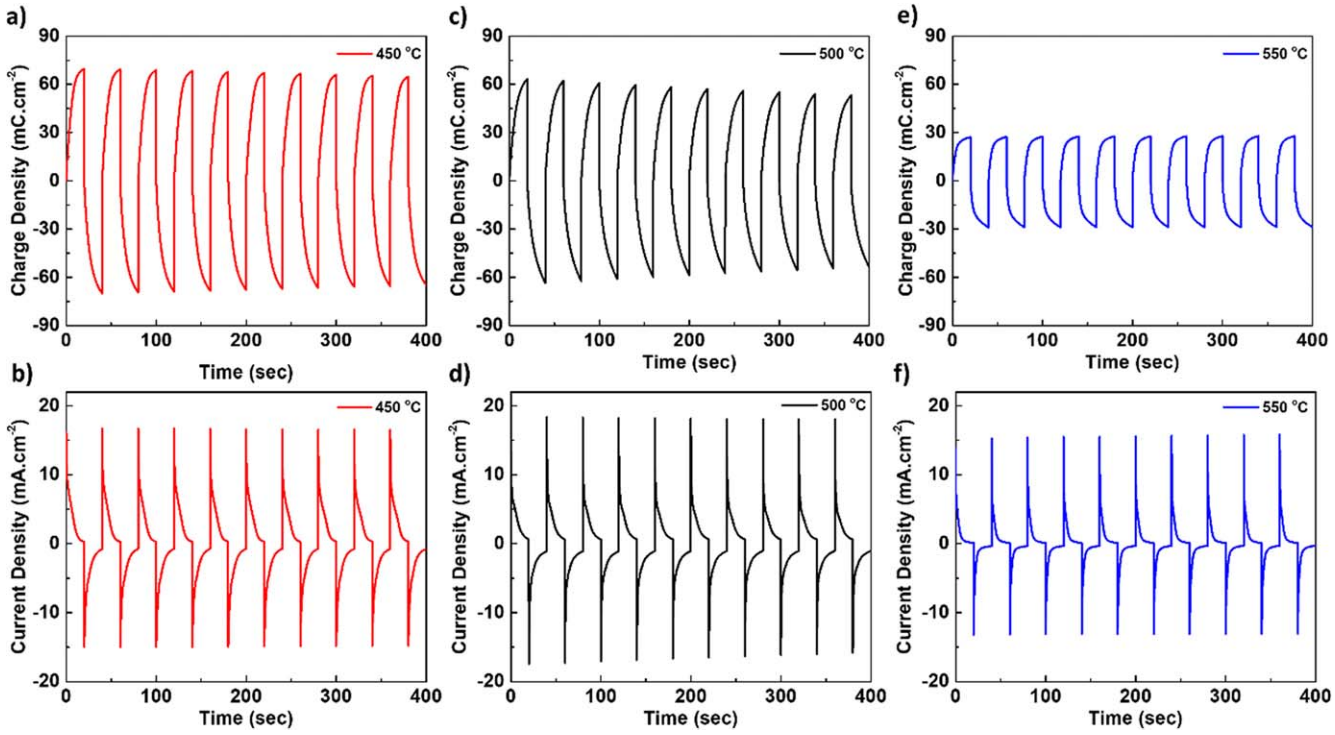

Figure 9. Chronocoulometric and chronoamperometric measurements for V_2O_5 samples annealed at (a), (b) 450, (c), (d) 500, and (e), (f) 550 °C.

Table III. A comparison of electrochromic parameters in terms of transmittance change, switching cycle life and wavelength. (*: This work).

Material	ΔT (%)	Switching Cycle Life	Wavelength (nm)	References
V_2O_5−450	17	over 25 cycles during 300 s	406	*
V_2O_5−500	15	over 25 cycles during 300 s	405	*
V_2O_5−550	4	over 25 cycles during 300 s	407	*
V_2O_5 Nanowires	37	3 cycles for 200 s	415	22
V_2O_5 Nanowires	36	200 cycles	400	86
V_2O_5 Nanowire Array	45	300 s	700	87
V_2O_5-Liquid Crystal	25	100 cycles during 1200 s	450	88

reversibility of the films in terms of charge efficiency can be calculated as the ratio of deintercalated charge (Q_{di}) to intercalated charge (Q_i) in the film as below:

$$Charge\ Efficiency = (Q_{di}/Q_i) \times 100$$

Charge efficiencies were calculated by averaging the charge densities of intercalation and deintercalation, and provided in Table IV. V_2O_5 film annealed at 450 °C showed the most promising result as the charge efficiency was approximately 99% with the highest intercalation and deintercalation charge densities reaching 67 mC.cm^{-2}.

CA curves of the thin films annealed at 450, 500, and 550 °C are also provided in Figs. 9b–9d–9f in tandem with the relevant CC figures. While the 500 °C annealed sample showed the highest deintercalation current densities, 450 °C annealed sample had

Table IV. Comparison of chronocoulometric data in terms of intercalation and deintercalation charge density.

Annealing Temperature	Intercalation Charge Density (mC.cm^{-2})	Deintercalation Charge Density (mC.cm^{-2})	Charge Efficiency (%)
450 °C	67.71 ± 1.45	67.12 ± 1.44	99.12 ± 0.08
500 °C	58.78 ± 2.94	57.05 ± 2.78	97.06 ± 1.07
550 °C	28.08 ± 0.08	27.65 ± 0.13	95.75 ± 0.70

broader charging and discharging curves. This also indicated that the accumulated charge densities during Li^+ insertion and extraction were higher for the 450 °C (**Fig. S5b**) annealed sample. All of these results support the transmittance changes provided in Fig. 7, confirming that the higher charge density and efficiency for the 450 °C annealed sample compared to the others, in line with the change in transmittance.

Following the electrochemical tests, thin-film electrodes were assembled into asymmetric electrochromic cells to monitor their cycling stability. Cyclic voltammograms of asymmetric electrochromic cells were obtained at a scan rate of 200 mV s^{-1} and provided in Fig. 10. Cyclic performance of the cells up to 1000 cycles is also given in Fig. 10. For all samples in Figs. 10a–10c, it is evident that the structure stabilizes and converges to a steady-state in the first 100 cycles such that the area within the cyclic voltammograms increases substantially up to 1000 cycles. The sample annealed at 450 °C showed promising CV characteristics in 3-electrode setup and showed the best performance and stability as can be seen from Figs. 10a and 10d. Moreover, Li^+ extraction voltage is lowered throughout the 1000 cycles as shown in Fig. 10a, which can be attributed to an enhanced Li^+ extraction capability.[76] This is probably due to the higher porosity, unique crystal (Fig. 1), vibrational (Fig. 2), electronic (Fig. 3) structure, and the finer nanorod morphology (Fig. 4) of the sample annealed at 450 °C as compared to the rest of the investigated samples. Continuous Li^+ intercalation/deintercalation within the structure increased the sample's activity through opening or activating new vanadium sites for the reaction, thus enhancing the electrochemical process. Lower intercalation voltage of the sample annealed at 450 °C compared to other samples after 1000 cycles can be seen in Fig. 10d, supporting this hypothesis.

Conclusions

In this work, homogeneous, crystalline, multichromic and single-phase V_2O_5 thin films were deposited using USD method onto FTO/glass substrates. As-deposited films were amorphous, while films annealed at 450 °C–550 °C showed the orthorhombic phase of V_2O_5. Microstructural and morphological analyses revealed that the average crystallite size of nanostructured films increased slightly from ∼20 to 22 nm upon increasing the annealing temperature. The optical band gaps of thin films were found to decrease from 2.69 to 2.58 eV with an increase in the annealing temperature. Hall-effect measurements showed that the deposited V_2O_5 thin films were *n*-type. Upon annealing the films, the carrier concentration was found to increase drastically, while mobility decreased only slightly. Raman and XPS results indicated that

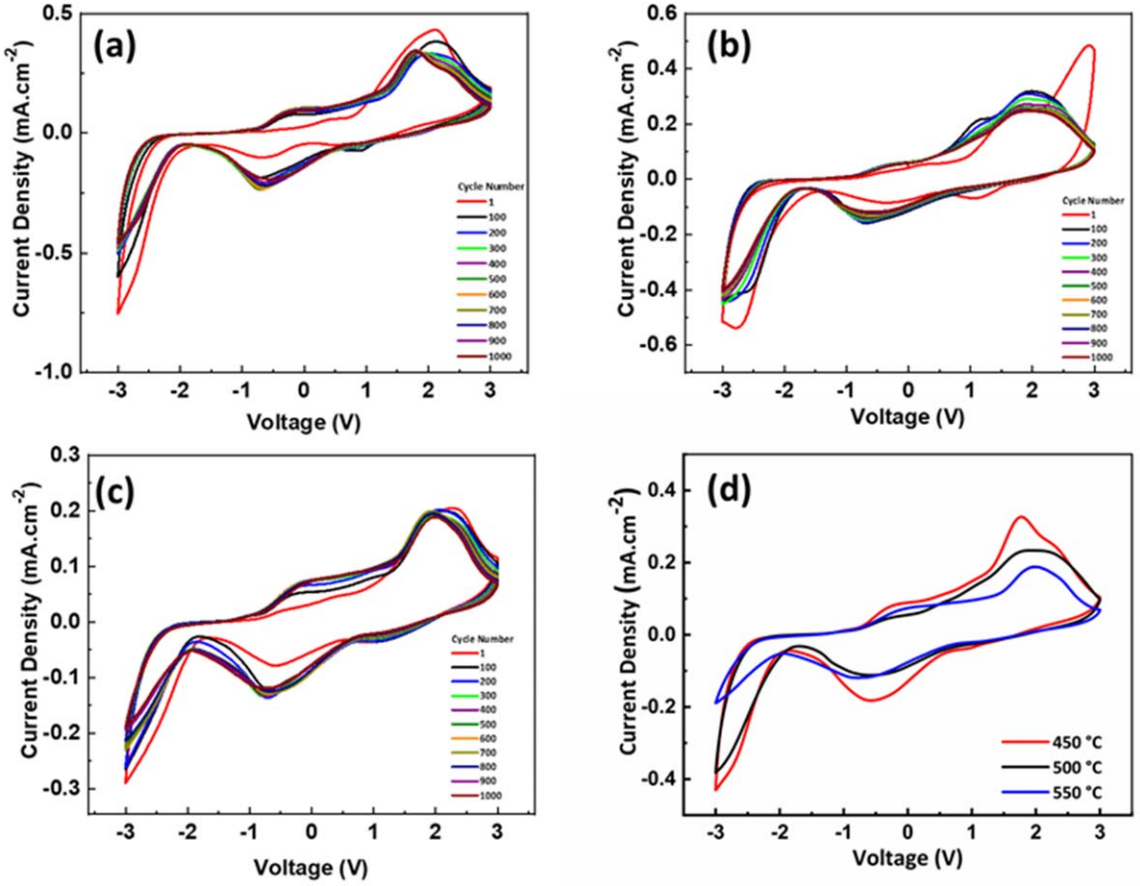

Figure 10. Cyclic voltammograms of asymmetric electrochromic cells at a scan rate of 200 mV s^{-1} for V_2O_5 samples annealed at (a) 450, (b) 500, and (c) 550 °C. (d) Cyclic voltammograms of the samples following 1000 cycles.

the best performing film (obtained at an annealing temperature of 450 °C) composed of predominantly V_2O_5 domains with a vanadium oxidation state of +5 in addition to the extremely small amount of minority species with V^{4+} states revealing decavanadate ($V_{10}O_{28}$) and/or isolated mono-oxovanadate (VO_4) surface functional groups. One of the highest diffusivities to date with a charging efficiency of 99% was reported. Homogeneous coloration with three different color states was observed for a large area (15 cm × 15 cm) V_2O_5 films upon electrochemical measurements. Electrochromic devices fabricated using V_2O_5/FTO electrodes annealed at 450 °C were found to be highly stable up to 1000 cycles. Our study clearly demonstrates that USD method is an extremely versatile technique for the deposition of uniform, reproducible, high quality, multichromic, and nanostructured V_2O_5 thin films over large areas using vanadium salt as a precursor solution.

Acknowledgments

This work was financially supported by the Middle East Technical University through the Scientific Research Projects Programme under project numbers YLT-308-2018-3738 and YLT-308-2018-3737. EO acknowledges the scientific collaboration with TARLA project founded by the Ministry of Development of Turkey (project code: DPT2006K-120470).

Declaration of Competing Interest

There are no conflicts to declare.

ORCID

Levent Toppare https://orcid.org/0000-0002-0198-4617
Husnu Emrah Unalan https://orcid.org/0000-0003-3667-179X

References

1. H. Su, S. Jaffer, and H. Yu, *Energy Storage Mater.*, **5**, 116 (2016).
2. J. Haber, M. Witko, and R. Tokarz, *Appl. Catal. A Gen.*, **157**, 3 (1997).
3. K. A. Gesheva, T. M. Ivanova, and G. Bodurov, *Prog. Org. Coatings*, **74**, 635 (2012).
4. K. Tang, Y. Zhang, Y. Shi, J. Cui, X. Shu, Y. Wang, Y. Qin, J. Liu, H. H. Tan, and Y. Wu, *Appl. Surf. Sci.*, **498**, 143796 (2019).
5. T.-S. Yang, Z.-R. Lin, and M.-S. Wong, *Appl. Surf. Sci.*, **252**, 2029 (2005).
6. S. Hou, A. I. Gavrilyuk, J. Zhao, H. Geng, N. Li, C. Hua, K. Zhang, and Y. Li, *Appl. Surf. Sci.*, **451**, 104 (2018).
7. J. Lin, S. Chen, and F. Kai, *Appl. Surf. Sci.*, **254**, 3357 (2008).
8. M. Dhanasankar, K. K. Purushothaman, and G. Muralidharan, *Appl. Surf. Sci.*, **257**, 2074 (2011).
9. O. Turel, S. O. Hacioglu, S. Coskun, L. Toppare, and H. E. Unalan, *J. Electrochem. Soc.*, **164**, E565 (2017).
10. K. Nagase, Y. Shimizu, N. Miura, and N. Yamazoe, *Appl. Phys. Lett.*, **60**, 802 (1992).
11. I. Mjejri, A. Rougier, and M. Gaudon, *Inorg. Chem.*, **56**, 1734 (2017).
12. I. Mjejri, M. Gaudon, and A. Rougier, *Sol. Energy Mater. Sol. Cells*, **198**, 19 (2019).
13. F. Ureña-Begara, A. Crunteanu, and J. P. Raskin, *Appl. Surf. Sci.*, **403**, 717 (2017).
14. G. S. Nadkarni and V. S. Shirodkar, *Thin Solid Films*, **105**, 115 (1983).
15. S. Beke, *Thin Solid Films*, **519**, 1761 (2011).
16. A. Z. Moshfegh and A. Ignatiev, *Thin Solid Films*, **198**, 251 (1991).
17. Z. Luo, Z. Wu, X. Xu, M. Du, T. Wang, and Y. Jiang, *Vacuum*, **85**, 145 (2010).
18. A. Dhayal Raj, T. Pazhanivel, P. Suresh Kumar, D. Mangalaraj, D. Nataraj, and N. Ponpandian, *Curr. Appl Phys.*, **10**, 531 (2010).
19. I. Raible, M. Burghard, U. Schlecht, A. Yasuda, and T. Vossmeyer, *Sensors Actuators, B Chem.*, **106**, 730 (2005).
20. J. Lichtenberger, *J. Catal.*, **223**, 296 (2004).
21. Z. Tong, N. Li, H. Lv, Y. Tian, H. Qu, X. Zhang, J. Zhao, and Y. Li, *Sol. Energy Mater. Sol. Cells*, **146**, 135 (2016).
22. K. C. Cheng, F. R. Chen, and J. J. Kai, *Sol. Energy Mater. Sol. Cells*, **90**, 1156 (2006).
23. J. Zhu, L. Cao, Y. Wu, Y. Gong, Z. Liu, H. E. Hoster, Y. Zhang, S. Zhang, S. Yang, Q. Yan, P. M. Ajayan, and R. Vajtai, *Nano Lett.*, **13**, 5408 (2013).
24. E. Umeshbabu and G. Ranga Rao, *J. Colloid Interface Sci.*, **472**, 210 (2016).
25. R. S. Ingole and B. J. Lokhande, *J. Mater. Sci., Mater. Electron.*, **27**, 1363 (2016).
26. R. Santos, J. Loureiro, A. Nogueira, E. Elangovan, J. V. Pinto, J. P. Veiga, T. Busani, E. Fortunato, R. Martins, and I. Ferreira, *Appl. Surf. Sci.*, **282**, 590 (2013).
27. I. Quinzeni, S. Ferrari, E. Quartarone, and P. Mustarelli, *J. Power Sources,*, **196**, 10228 (2011).
28. L. J. Meng, R. A. Silva, H. N. Cui, V. Teixeira, M. P. dos Santos, and Z. Xu, *Thin Solid Films*, **515**, 195 (2006).
29. C. V. Ramana, R. J. Smith, O. M. Hussain, C. C. Chusuei, and C. M. Julien, *Chem. Mater.*, **17**, 1213 (2005).
30. C. Julien, E. Haro-Poniatowski, M. A. Camacho-López, L. Escobar-Alarcón, and J. Jímenez-Jarquín, *Mater. Sci. Eng. B Solid-State Mater. Adv. Technol.*, **65**, 170 (1999).
31. P. K. Jain, M. Salim, and D. Kaur, *Optik (Stuttg).*, **126**, 3260 (2015).
32. D. Vernardou, *Coatings*, **7**, 1 (2017).
33. D. Barreca, L. E. Depero, E. Franzato, G. A. Rizzi, L. Sangaletti, E. Tondello, and U. Vettori, *J. Electrochem. Soc.*, **146**, 551 (1999).
34. N. K. Nandakumar and E. G. Seebauer, *Thin Solid Films*, **519**, 3663 (2011).
35. O. Monfort, T. Roch, L. Satrapinskyy, M. Gregor, T. Plecenik, A. Plecenik, and G. Plesch, *Appl. Surf. Sci.*, **322**, 21 (2014).
36. Y. Ningyi, L. Jinhua, and L. Chenglu, *Appl. Surf. Sci.*, **191**, 176 (2002).
37. R. S. Ingole and B. J. Lokhande, *Mater. Lett.*, **168**, 95 (2016).
38. R. Irani, S. M. Rozati, and S. Beke, *Mater. Chem. Phys.*, **139**, 489 (2013).
39. M. Abbasi, S. M. Rozati, R. Irani, and S. Beke, *Mater. Sci. Semicond. Process.*, **29**, 132 (2015).
40. Y. Wei, M. Li, J. Zheng, and C. Xu, *Thin Solid Films*, **534**, 446 (2013).
41. I. J. Tadeo, R. Parasuraman, S. B. Krupanidhi, and A. M. Umarji, *Nano Express*, **1**, 010005 (2020).
42. Z. Chen, Y. Tang, A. Ji, L. Zhang, and Y. Gao, *ACS Appl. Nano Mater.*, **4**, 4048 (2021).
43. R. Ramarajan, M. Kovendhan, K. Thangaraju, D. P. Joseph, and R. R. Babu, *Appl. Surf. Sci.*, **487**, 1385 (2019).
44. S. Y. Wang, W. Wang, W. Z. Wang, and Y. W. Du, *Mater. Sci. Eng. B Solid-State Mater. Adv. Technol.*, **90**, 133 (2002).
45. J. Denayer, G. Bister, P. Simonis, P. Colson, A. Maho, P. Aubry, B. Vertruyen, C. Henrist, V. Lardot, F. Cambier, and R. Cloots, *Appl. Surf. Sci.*, **321**, 61 (2014).
46. R. C. Tenent, D. T. Gillaspie, A. Miedaner, P. A. Parilla, C. J. Curtis, and A. C. Dillon, *J. Electrochem. Soc.*, **157**, H318 (2010).
47. D. Chatzikyriakou, A. Maho, R. Cloots, and C. Henrist, *Microporous Mesoporous Mater.*, **240**, 31 (2017).
48. J. Denayer, P. Aubry, G. Bister, G. Spronck, P. Colson, B. Vertruyen, V. Lardot, F. Cambier, C. Henrist, and R. Cloots, *Sol. Energy Mater. Sol. Cells*, **130**, 623 (2014).
49. C. P. Li, F. Lin, R. M. Richards, C. Engtrakul, R. C. Tenent, and C. A. Wolden, *Sol. Energy Mater. Sol. Cells*, **121**, 163 (2014).
50. C. P. Li, C. A. Wolden, A. C. Dillon, and R. C. Tenent, *Sol. Energy Mater. Sol. Cells*, **99**, 50 (2012).
51. K. Jeyalakshmi, S. Vijayakumar, S. Nagamuthu, and G. Muralidharan, *Mater. Res. Bull.*, **48**, 760 (2013).
52. G. J. Fang, Z. L. Liu, Y. Q. Wang, H. H. Liu, and K. L. Yao, *J. Phys. D: Appl. Phys.*, **33**, 3018 (2000).
53. A. Šurca and B. Orel, *Electrochim. Acta*, **44**, 3051 (1999).
54. N. Özer, *Thin Solid Films*, **305**, 80 (1997).
55. S. Beke, S. Giorgio, L. Korösi, L. Nánai, and W. Marine, *Thin Solid Films*, **516**, 4659 (2008).
56. G. K. Williamson and W. H. Hall, *Acta Metall.*, **1**, 22 (1953).
57. G. K. Williamson and R. E. Smallman, *Philos. Mag.*, **1**, 34 (1956).
58. R. Baddour-Hadjean, J. P. Pereira-Ramos, C. Navone, and M. Smirnov, *Chem. Mater.*, **20**, 1916 (2008).
59. J. Strunk, M. A. Bañares, and I. E. Wachs, *Vibrational Spectroscopy of Oxide Overlayers* (Springer Berlin, US) 1577 (2017).
60. G. Deo and I. E. Wachs, *J. Phys. Chem.*, **95**, 5889 (1991).
61. N. Das, H. Eckert, H. Hu, I. E. Wachs, J. F. Walzer, and F. J. Feher, *J. Phys. Chem.*, **97**, 8240 (1993).
62. H. Tian, E. I. Ross, and I. E. Wachs, *J. Phys. Chem. B*, **110**, 9593 (2006).
63. G. Beamson, N. Moslemzadeh, P. Weightman, and J. F. Watts, *J. Electron Spectros. Relat. Phenomena*, **162**, 19 (2008).
64. R. Zimmerman, R. Claessen, F. Reinert, P. Steiner, and S. Hufner, *J. Phys.: Condens. Matter,*, **10**, 5697 (1998).
65. J. Mendialdua, R. Casanova, and Y. Barbaux, *J. Electron Spectros. Relat. Phenomena*, **71**, 249 (1995).
66. G. Silversmit, D. Depla, H. Poelman, G. B. Marin, and R. De Gryse, *J. Electron Spectros. Relat. Phenomena*, **135**, 167 (2004).
67. M. Demeter, M. Neumann, and W. Reichelt, *Surface Science*, **456**, 41 (2000).
68. E. Cazzanelli, G. Mariotto, S. Passerini, W. H. Smyrl, and A. Gorenstein, *Sol. Energy Mater. Sol. Cells*, **56**, 249 (1999).
69. S. H. A. Ahmad, M. F. Al-Kuhaili, S. M. A. Durrani, M. M. Faiz, and A. Ul-Hamid, *Sol. Energy Mater. Sol. Cells*, **169**, 258 (2017).
70. J. E. N. Swallow, B. A. D. Williamson, T. J. Whittles, M. Birkett, T. J. Featherson, N. Peng, A. Abbot, M. Farnworth, K. J. Cheetham, P. Warren, D. O. Scanlon, V. R. Dhanak, and T. D. Veal, *Adv. Funct. Mater.*, **28**, 1 (2018).
71. Y. Qu, T. A. Gessert, K. Ramanathan, R. G. Dhere, R. Noufi, and T. J. Coutts, *J. Vac. Sci. Technol. A Vacuum, Surfaces, Film.*, **11**, 996 (1993).
72. S. S. Lin and J. L. Huang, *Ceram. Int.*, **30**, 497 (2004).
73. V. Yelsani, N. Pothukanuri, U. B. Sontu, V. Yaragani, and R. R. Musku Venkata, *Medziagotyra*, **25**, 3 (2019).
74. K. Jeyalakshmi, S. Vijayakumar, S. Nagamuthu, and G. Muralidharan, *Mater. Res. Bull.*, **48**, 760 (2013).
75. C. V. Ramana, R. J. Smith, and O. M. Hussain, *Phys. Status Solidi Appl. Res.*, **199**, 5 (2003).
76. Y. Wei, J. Zhou, J. Zheng, and C. Xu, *Electrochim. Acta*, **166**, 277 (2015).
77. C. Xiong, A. E. Aliev, B. Gnade, and K. J. Balkus, *ACS Nano*, **2**, 293 (2008).

78. I. Mjejri, M. Gaudon, G. Song, C. Labrugère, and A. Rougier, *ACS Appl. Energy Mater.*, **1**, 2721 (2018).
79. M. Benmoussa, A. Outzourhit, A. Bennouna, and E. L. Ameziane, *Thin Solid Films*, **405**, 11 (2002).
80. C. Xiong, A. E. Aliev, B. Gnade, and K. J. Balkus, *ACS Nano*, **2**, 293 (2008).
81. Y. Qi, K. Qin, Y. Zou, L. Lin, Z. Jian, and W. Chen, *Appl. Surf. Sci.*, **514**, 145950 (2020).
82. M. Panagopoulou, D. Vernardou, E. Koudoumas, N. Katsarakis, D. Tsoukalas, and Y. S. Raptis, *J. Phys. Chem. C*, **121**, 70 (2017).
83. X. Li, C. Liu, C. Zhang, H. Fu, X. Nan, W. Ma, Z. Li, K. Wang, H. Wu, and G. Cao, *ACS Appl. Mater. Interfaces*, **8**, 24629 (2016).
84. J. Huotari, R. Bjorklund, J. Lappalainen, and A. Lloyd Spetz, *Sensors Actuators, B Chem.*, **217**, 22 (2015).
85. D. Raj, D. Mangalaraj, N. Ponpandian, and J. Yi, *Adv. Mater. Res.*, **123–125**, 683 (2010).
86. Y. Sen Lin and C. W. Tsai, *Surf. Coatings Technol.*, **202**, 5641 (2008).
87. K. Takahashi, Y. Wang, and G. Cao, *Appl. Phys. Lett.*, **86**, 1 (2005).
88. U. Tritschler, F. Beck, H. Schlaad, and H. Cölfen, *J. Mater. Chem. C*, **3**, 950 (2015).